

Research Article

Surface Shape Detection with a Single Far-Field Intensity by Combined Amplitude and Phase Retrieval

Huiliang Jin¹, Jianhui Huang¹, Qian Ye¹, Guoxiang Meng¹, Binbin Xiang¹,² and Na Wang²

¹School of Mechanical Engineering, Shanghai Jiao Tong University, Shanghai 200240, China

²XinJiang Astronomical Observatory, CAS, Ürümqi 830011, China

Correspondence should be addressed to Huiliang Jin; hljin@sjtu.edu.cn

Received 6 March 2019; Revised 17 May 2019; Accepted 26 June 2019; Published 18 August 2019

Academic Editor: Giorgio Montisci

Copyright © 2019 Huiliang Jin et al. This is an open access article distributed under the Creative Commons Attribution License, which permits unrestricted use, distribution, and reproduction in any medium, provided the original work is properly cited.

The efficiency of a reflector antenna highly depends on its surface shape. In order to ensure a good convergence, the conventional phase retrieval based shape detection schemes require that several far-field intensities be scanned, focused, or defocused. For large reflector antennas, the scanning process is time consuming. This paper proposes a new shape detection method that requires only single far-field intensity. Unlike existing shape detection methods, it retrieves both the amplitude and the phase, based on the fact that a deformed shape causes change not only in the aperture phase but also in the aperture amplitude. Through even-odd decomposition analysis, it is found that in the case of small and smooth deformation, “odd-phase” and “even-amplitude” can be directly recovered from one focused far-field intensity. This leads to the recovery of both the odd and the even parts of the antenna surface shape simultaneously. By combining amplitude retrieval and phase retrieval, this work achieves for the first time the shape detection with only one scan.

1. Introduction

Within years, a 110 m radio telescope named QTT will be built in QiTai, Xinjian, China. Its huge reflector is assembled from thousands of panels, under which precision actuators are installed at the corners. The actuators are applied to compensate for surface deformation errors caused mainly by gravity, wind, and temperature and keep the deformed surface to an ideal paraboloid. QTT works at the frequency between 0.15~115 GHz. Ruze [1] pointed out that the efficiency of reflector antennas depends on its surface shape accuracy. To achieve acceptable efficiency, surface errors RMS should be less than 0.2 mm ($\lambda/16$) for 100 GHz observation. The challenge now is to measure the shape quickly and effectively. Closely related to the surface shape accuracy is the problem of phase retrieval. Rahmat-Samii [2] derived a linear mapping between the surface shape and its radiated aperture field phase. This mapping indicates that surface shape detection is equivalent to a phase retrieval problem.

In the past decades, phase retrieval has attracted considerable interest and has been continuously studied in the field of shape detection for large antennas [3]. Researchers, on one hand, concentrated on improving the traditional phase retrieval algorithms such as the Misell algorithm [4] and on the other hand developed new algorithms, such as the global optimization algorithms [5]. These efforts lead to a more accurate phase recovery. However, most of them still require several far-field scans, usually the focused, the positive, and negative defocused [6, 7]. For huge reflector antennas, multiple-scan is time consuming and laborious.

It is helpful to study the phase retrieval with a single far-field intensity so that the measurement procedure can be greatly simplified. By means of even-odd decomposition, Gonsalves [8] showed that under the “small phase” assumption, the odd part of the phase can be directly solved from the focused far-field image. However, the even part cannot be uniquely determined without further observations. Following a similar way, Li et al. [9] showed that the even part

of the phase can also be solved directly, provided that the phase aberration in the system is “even and small.” By using a linear approximation, Dong et al. [10] and Polo et al. [11] proposed a method with a single defocused far-field image for small aberrations. They showed that the focused image reflects little messages of the even phase aberration, and the defocused images would reflect much more if the off-focus distance is appropriate.

In this paper, a noniterative shape detection method is developed. The method is efficient as it requires a single scan of the focused far-field intensity. A schematic diagram is shown in Figure 1. The algorithm is based on the fact that shape deformation causes changes not only in the phase but also in the amplitude. Unlike traditional methods, it also retrieves the amplitude during the phase retrieval process. Through theoretical analysis and numerical simulations, it is demonstrated that complete recovery of surface shape deformation with only one scanned in-focus far-field intensity is possible.

2. Problem Setup and Definition

The problem is defined and solved under the following assumptions:

- (A.1) Low test frequency: the frequency is assumed to be $f < 1 \text{ GHz}$.
- (A.2) The deformation is small: the deformation δ is considered small (a few millimeters), to be exact, $E < 0.1$, $C < 0.01$.
- (A.3) The deformation is smooth: δ is considered second-order smooth so that differential calculations are always accurate.

Among the above three assumptions, “low test frequency” is the necessary precondition to conduct the proposed scheme, and the last two assumptions are actually the physical truth of real large radio telescopes. In this case, the surface deformation is always very tiny due to fine fabrication and assemblage. In addition, from Figure 1 in reference [12], the antenna surface deformation is caused by the displacement of the actuators installed under reflector panels. From mechanics of the antenna structure, the surface deformation caused by gravity, wind, and temperature is second-order smooth. Therefore, δ is naturally smooth and has a small range. These are the facts of real radio telescopes but not just assumptions.

Symbols involved are listed in Table 1. To simplify the analysis, only the deformation in the primary reflector is investigated.

When the antenna surface shape deforms, both the phase and the amplitude of the radiated aperture field are disturbed. Let the ideal aperture field be denoted by $B(x, y)$, with the phase being uniformly zero. Assume that the surface deformation $\delta(x, y)$ causes an aberration $E(x, y)$ in the phase, together with a relative increase $C(x, y)$ in the amplitude so that $B \cdot C$ is the variation in the amplitude. The coordinates (x, y) shall be omitted hereinafter to make a concise expression of the mathematic formulas. Based on these assumptions,

the aperture distribution A under surface deformation is complex valued and can be expressed as

$$A = |A|e^{iE} = B(1 + C)e^{iE}. \quad (1)$$

For large reflector antennas, the far-field radiation equals the Fourier transformation of its aperture field. Let the far-field radiation under surface deformation and the ideal far-field radiation be denoted by $a(u, v)$ and $b(u, v)$, respectively. These far-field radiations are uniquely determined by the aperture distributions as follows:

$$\begin{aligned} a &= F(A) = F(|A|e^{iE}), \\ b &= F(B), \end{aligned} \quad (2)$$

where F represents the 2D Fourier transformation.

In the above, the ideal aperture amplitude B is usually assumed to be real and even. According to the properties of the Fourier transformation, the corresponding far-field amplitude b is real and even too. Both b and B can be prepared in advance and therefore assumed to be known. Specifically, an ideal far-field pattern is the radiation field of an antenna with radial symmetric feed pattern and standard parabolic reflector. Generally, the feed is precisely made so that the pattern is naturally radial symmetric, and the reflector can be adjusted to be a standard paraboloid by existing antenna detection techniques. Only the radiated far-field intensity under surface deformation will be measured.

We are to find a method to determine the antenna surface shape deformation from its radiated far-field intensity only. To solve this problem, two important relationships between the deformation, the aperture amplitude, and the aperture phase are required, playing the key role toward the solution. The first one is the so-called phase-deformation relationship, obtained by Rahmat-Samii [2]. It relates the aperture phase linearly with the surface deformation as shown in the following equation:

$$E = \frac{8F_L^2 k}{x^2 + y^2 + 4F_L^2} \cdot \delta, \quad (3)$$

where F_L and k denote the focal length and the wavenumber, respectively. The second one is the so-called deformation-amplitude relationship. Developed in our earlier work [12], it sets up a linear mapping between the aperture amplitude and the surface deformation as follows:

$$\delta = F^{-1} \left(\frac{F[C/G]}{F(L_N)} \right), \quad (4)$$

where G is a characteristic matrix determined by antenna geometry and L_N is the Laplacian matrix extended to size $N \times N$ by zero-padding. Readers are referred to [12] for more details.

For a shorter expression, the above two relationships are rewritten as

$$\begin{aligned} \delta &= \Phi \cdot E, \\ \delta &= \Psi(C), \end{aligned} \quad (5)$$

where the matrix Φ and the function Ψ are also known. These two relationships indicate that the problem of surface shape detection can be solved by either one of them, i.e., by

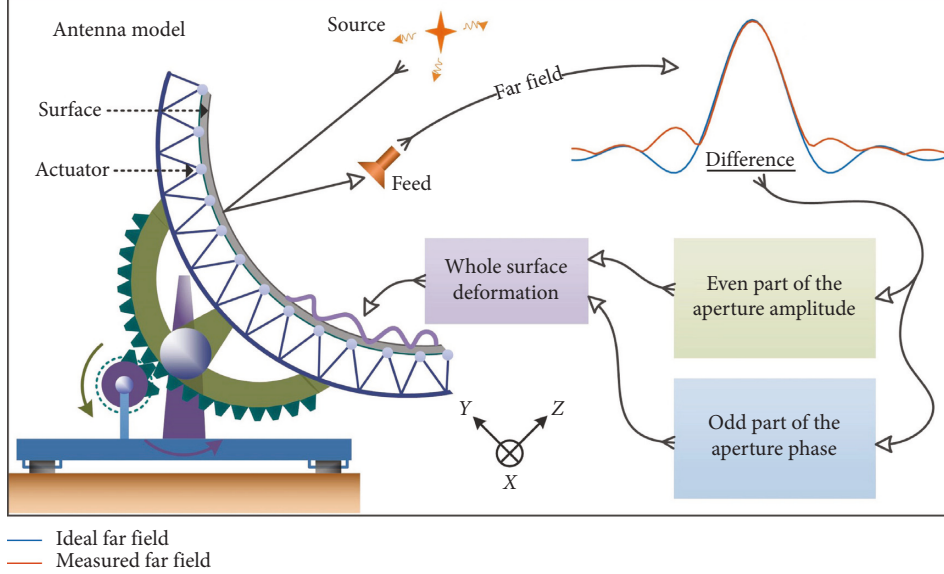


FIGURE 1: Schematic diagram of the surface shape detection method with only one in-focus far-field intensity, based on even-odd decomposition.

retrieving either the phase E or the amplitude C . Most of the existing methods rely on the former, and the phase retrieval algorithms involved require several recorded far-field intensities. On the contrary, the current work proposes a new approach to complete shape reconstruction with a single focused far-field intensity measurement. This is achieved by retrieving both C and E , or more specifically, by recovering the odd part of E and the even part of C , from the measured single far-field amplitude $|a|$.

It should be noted that the problem involved is not a regular 2D phase retrieval problem; since C and E are not independent, they both depend upon the deformation δ by equation (5). Retrieval of δ from a single far-field amplitude $|a|$ is possible, as the amount of information contained in both of them is the same.

3. Solution (Main Result)

3.1. Amplitude-Phase Retrieval. Every function can be uniquely decomposed into the sum of an even part and an odd part. In the following, the subscripts “*e*” and “*o*” are used to indicate the even part and the odd part, respectively. The complex-valued aperture distribution A in equation (1) can be expressed as

$$A = B(1 + C_e + C_o)(\cos(E_e + E_o) + i \sin(E_e + E_o)). \quad (6)$$

It can be decomposed into four parts: the real-even part, the real-odd part, the imaginary-even part, and the imaginary-odd part. Note that $C \ll E \ll 1$, by first order Taylor expansion,

$$\left\{ \begin{array}{l} A_{re} = B(1 + C_e)\cos E_e \cos E_o - BC_o \sin E_e \sin E_o \sim B(1 + C_e), \\ A_{ro} = BC_o \cos E_e \cos E_o - B(1 + C_e)\sin E_e \sin E_o \sim BC_o, \\ A_{ie} = B(1 + C_e)\sin E_e \cos E_o + BC_o \cos E_e \sin E_o \sim BE_e, \\ A_{io} = B(1 + C_e)\cos E_e \sin E_o + BC_o \sin E_e \cos E_o \sim BE_o. \end{array} \right. \quad (7)$$

TABLE 1: List of symbols.

| Symbol | Unit | Meaning |
|-------------|------|---|
| a | | Far field of the tested antenna, complex-valued |
| A | | Aperture field of the tested antenna, complex-valued |
| b | | Far-field amplitude of an ideal antenna, real and even |
| B | | Aperture amplitude of an ideal antenna, real and even |
| C | | Relative aperture amplitude increase caused by δ |
| E | rad | Aperture phase aberration caused by δ |
| f | GHz | Frequency of the source in the measurement |
| F, F^{-1} | | FFT, inverse FFT |
| F_L | m | Focal length of tested antenna |
| G | | A matrix determined by antenna geometry [12] |
| k | | Wavenumber |
| L_N | | Laplacian matrix extended to size $N \times N$ [12] |
| N | | Data size $N \times N$ |
| δ | mm | Surface shape error of the tested antenna |
| η | | Oversampling factor in the far-field scanning |

This shows that the aperture field is dominated by the real-even part. The corresponding far-field pattern is

$$a = F(A) = \underbrace{\overline{F(A_{re})}}_{\text{the real part, dominant}} + \underbrace{\overline{F(iA_{io})}}_{\text{neglectable}} + \underbrace{F(A_{ro}) + F(iA_{ie})}_{\text{imaginary part, neglectable}}. \quad (8)$$

According to the theories of the Fourier transformation, $F(A_{re})$ is real and even, but $F(iA_{io})$ is real and odd. Equation (8) indicates that the far-field pattern a is dominated by the real part. It also implies that the following equation is approximately satisfied:

$$a \approx a_r = |a| \cdot \cos \angle a \approx |a| \cdot \text{sign}(b), \quad (9)$$

where “ \angle ” means taking the phase and “ sign ” is the signum function. By combining equations (7)–(9), one obtains

$$\begin{cases} |a|_e \operatorname{sign}(b) \approx F(A_{re}) \approx F(B(1 + C_e)) = b + F(BC_e), \\ |a|_o \operatorname{sign}(b) \approx F(iA_{io}) \approx iF(BE_o). \end{cases} \quad (10)$$

From this equation, both C_e and E_o can be easily solved as

$$\begin{cases} C_e \approx \frac{F^{-1}[|a|_e \operatorname{sign}(b) - b]}{B}, \\ E_o \approx \frac{F^{-1}[-i \cdot |a|_o \operatorname{sign}(b)]}{B}. \end{cases} \quad (11)$$

Finally, by using equation (5), the overall surface deformation δ can be solved as

$$\delta = \delta_e + \delta_o = \Psi(C_e) + \Phi \cdot E_o. \quad (12)$$

It should be remarked that an alternative solution may also be obtained from the equation below:

$$|a|^2 = \underbrace{[F(A_{re}) + F(iA_{io})]^2}_{\text{the real part of } a, \text{ dominant}} + \underbrace{[F(A_{ro}) + F(iA_{ie})]^2}_{\text{neglectable}}. \quad (13)$$

By following the similar analysis as in [8, 9] and neglecting some insignificant terms in the above, one obtains

$$\begin{aligned} |a|^2 &\approx F(A_{re})^2 + 2F(A_{re})F(iA_{io}) \\ &\approx \underbrace{F(B)^2 + 2F(B)F(BC_e)}_{\text{even}} + \underbrace{2F(B)F(iBE_o)}_{\text{odd}}, \end{aligned} \quad (14)$$

from which C_e and E_o can be solved as

$$\begin{aligned} C_e &= \left(\frac{1}{B}\right)F^{-1}\left(\frac{|a|_e^2 - b^2}{2b}\right), \\ E_o &= \left(\frac{1}{iB}\right)F^{-1}\left(\frac{|a|_o^2}{2b}\right). \end{aligned} \quad (15)$$

In comparison with this solution, equation (11) generally does not exhibit higher reconstruction accuracy in the case of large aperture phase as a result of rougher approximation introduced. However, when the aperture phase E is small, equation (11) usually gives better results for recovery of E_o as it does not involve division by b . Since b is similar to the Bessel function of the first kind of first order, it contains a great number of points of zero or close to zero so that division by b would amplify greatly the noises or errors.

3.2. Algorithm Flow. Figure 2 shows the flow chart of the algorithm, with the measured far-field $|a|$ as the input and the shape recovery δ_r as the output. For a simpler expression, an auxiliary variable d is introduced to denote the far-field difference:

$$d \triangleq |a| \cdot \operatorname{sign}(b) - b. \quad (16)$$

From the point of numerical calculation, it should be noted that there may be some wrong data with opposite sign in the subtraction calculation of equation (16). A median filter may correct the wrong data properly since it is smooth originally. For numerical calculation of the Fourier

transformation, it should also be noted that the distributions in the spatial domain should be expanded by zero-padding to ensure a suitable size. This may be controlled by the oversampling factor η .

4. Simulations

4.1. Effectiveness of the Method. In this study, numerical simulation is adopted to verify the validity and testify other performance of the proposed method. Primary steps of the simulation are as follows:

- (1) Generate randomly a smooth surface shape deformation δ
- (2) Calculate the radiated aperture field A by physical optics
- (3) Obtain the far-field amplitude $|a|$ according to equation (2)
- (4) Recover δ from $|a|$ by the algorithm as shown in Figure 2
- (5) Compare the retrieved shape δ_r with the given δ

In Step (1), the surface shape deformation δ is designed to be randomly smooth, for the reason that the antenna surface deformation is a combination effect of gravity, wind, and temperature. The deformation caused by these factors is always smooth. In Step (2), the physical optics (PO) method [13] is used to calculate the radiated aperture field. Based on the Maxwell equations, the PO method is widely used and regarded as an accurate theory in the field of antenna radiation.

In consideration of future experimental verification, we take Nanshan 25 m radio telescope (25 m diameter and 7.5 m focal length, Urumqi, Xinjiang) as the antenna model. PO is applied to simulate its radiated aperture field, with the parameters listed in Table 2.

To evaluate the accuracy of the recovered final results, two standard performance indices, i.e., root mean square (RMS) error and normalized mean-square-error (NMSE), are introduced. Specifically,

$$\begin{aligned} \text{RMS} &= \frac{\|f_r - f\|_F}{N}, \\ \text{NMSE} &= \frac{\|f_r - f\|_F^2}{\|f\|_F^2}, \end{aligned} \quad (17)$$

where f_r represents the recovered matrix (or distribution), f , the target to be recovered, and $\|\cdot\|_F$ is the Frobenius norm of a matrix.

Figure 3 shows a designed surface error δ (left of top line). It is randomly generated but smooth, having a range of $[-1, 1]$ mm, which is close to the real case.

The Fourier transformation in equation (2) is used to calculate the far-field intensity. To satisfy Nyquist sampling theorem, the oversampling factor η must be no less than 2. Here, η is set to 4 to ensure a smooth far-field pattern, in which the far-field is with the size 405×405 . Following the algorithm depicted in Figure 2, we reconstruct C_e and E_o

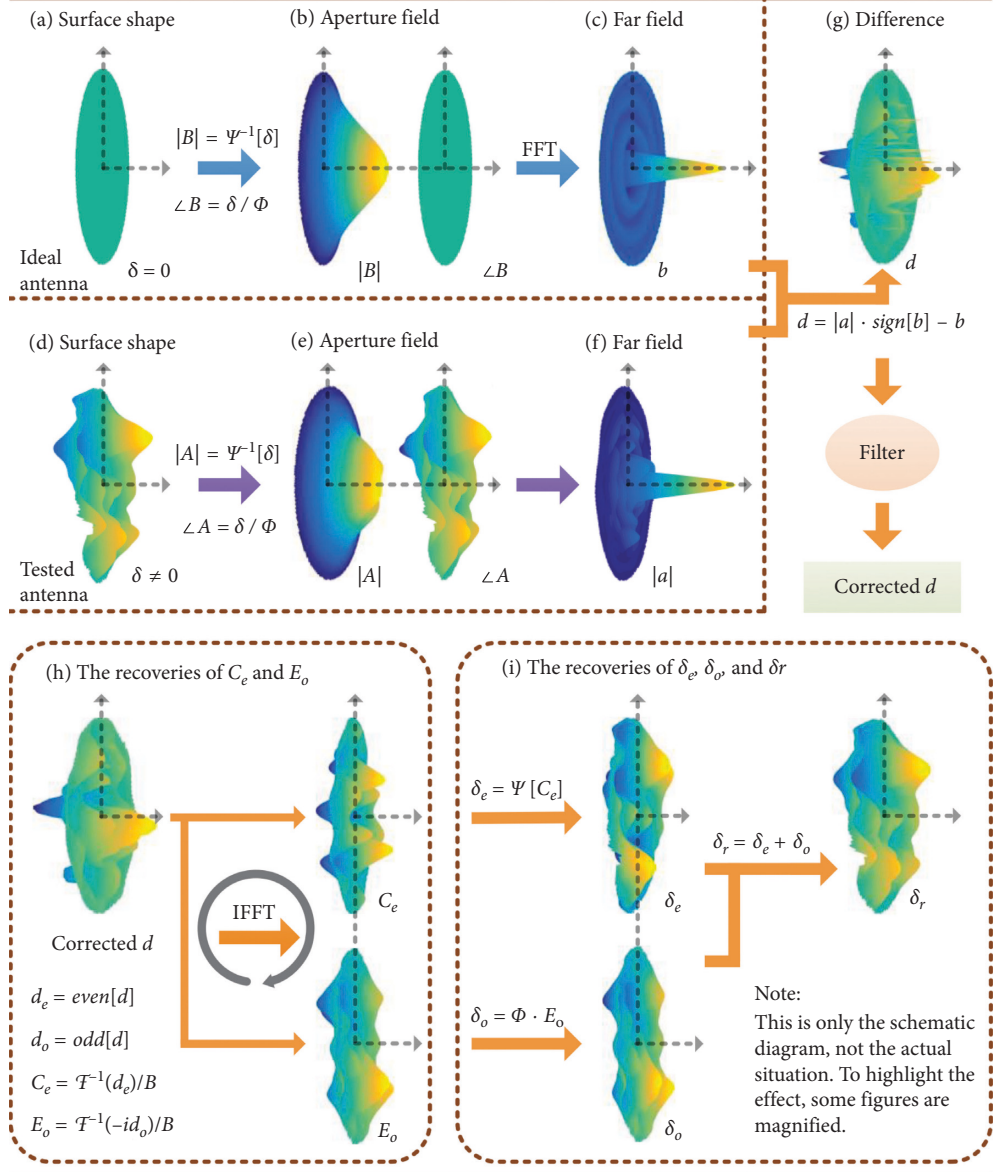


FIGURE 2: Flow chart of the surface shape recovery algorithm, with a single in-focus far-field amplitude as the input. The ideal far-field amplitude is assumed to be known in advance.

TABLE 2: Parameters in the PO method for aperture field simulation.

| δ | Frequency | Feed beam | Edge taper | N |
|--------------|-----------|-----------|------------|-----|
| $[-1, 1]$ mm | 0.3 GHz | Gaussian | -12 dB | 101 |

from $|a|^2$ in a closed-form way and further determine the complete surface shape δ .

The recovered results are also shown in Figure 3. An acceptable shape recovery with the RMS value less than 0.14 mm is achieved. However, the difference between δ_r and δ is still observable: the peaks and valleys become fuzzy. This can be explained by the following two reasons. First, equation (4) is not absolutely accurate for it calculates the near field radiation of an antenna in pure geometric way. Second, equation (9) is also an approximate relation and results in errors inevitably.

4.2. Accuracy Performance. In the above derivation, the core step is to recover C_e and E_o . Since all the equations are established under the assumption of a small C and E , a smaller range of C and E will lead in general to a higher accuracy of the method. It is necessary to investigate the accuracy of the amplitude-phase retrieval at different ranges of C and E by a series of numerical simulations. In the simulations, B is defined with the shape of plane, valued by 1. C and E are both generated with a randomly smooth shape, as shown in Figure 4.

Usually a recovered result with NMSE below a certain level, say 0.1 for example, can be regarded as acceptable in engineering. Figure 5 shows the recovery accuracy of C_e and E_o under different ranges of C and E . The figure indicates that acceptable recovery of C_e is achieved under the condition: $0 < E < C < 0.6$; acceptable recovery to E_o is achieved under a more tolerant condition: $C < 0.6$ and $E < 1$.

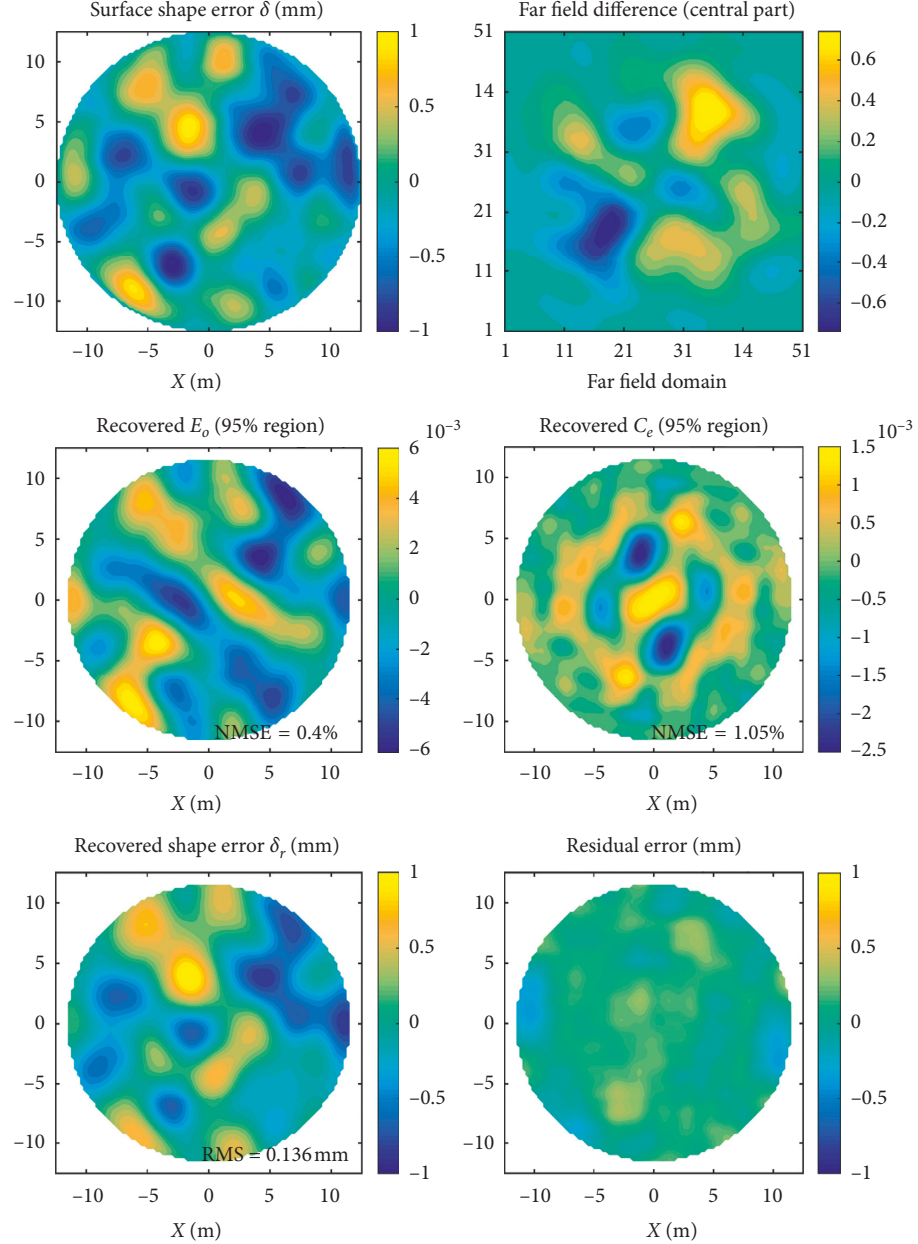


FIGURE 3: The top line: the designed surface shape error (left) and the simulated far-field difference (right). The middle line: the recoveries to E_o and C_e , with the NMSE values being 0.40% and 1.05%, respectively. The bottom line: the final retrieved surface shape error (left) and the residual error map (right).

4.3. Performance under Different Frequencies. To study the performance of the new method under different test frequencies, the PO method is employed to simulate many far-field intensities under different frequencies, from which we obtained shape detection with different accuracy. The results are listed in Table 3. A higher test frequency means $E \gg C$ and definitely leads to a worse recovery. It can be predicted from Figure 5 that with the increase of the test frequency, E becomes much larger than C and the recovery to C_e gets worse rapidly. Therefore, a low-frequency test is always preferred.

Finally, it should be remarked that “test frequency” and “work frequency” are totally two different things. A radio telescope may work at a frequency as high as 100 GHz.

However, this requires in no way that the test should be conducted at the same frequency of 100 GHz. The test may be conducted at any frequency below 100 GHz, as long as the measurement accuracy meets the engineering requirement.

4.4. Performance under Feed Errors. This section discusses the performances of the proposed technique under a wrong feed positioning and Gaussian noise mixed into the measured far-field intensity data. In the simulation, the coordinate system of the feed is defined by X , Y , and Z axes, where X - Y indicates a plane parallel to that antenna aperture, and Z direction follows the pointing angle of the telescope.

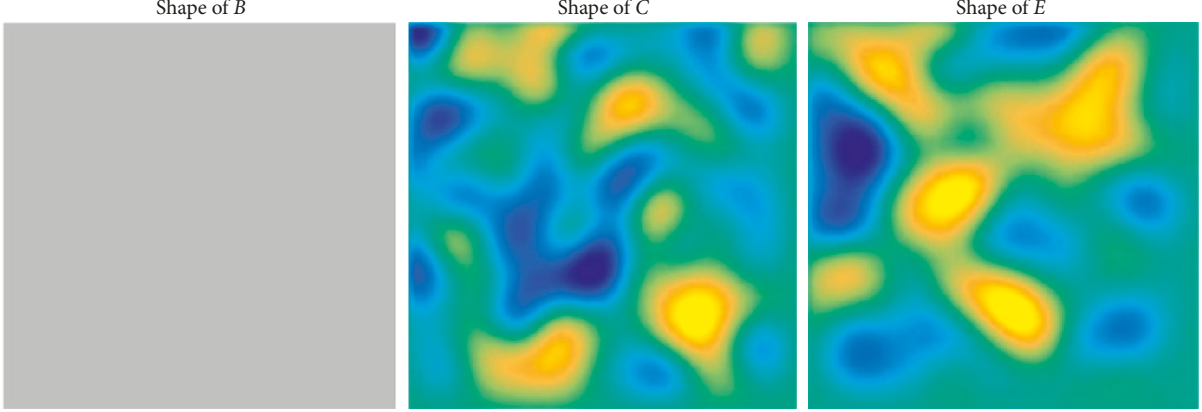


FIGURE 4: Shapes of B , C , and E : both C and E are set to be randomly smooth and B is set to be a constant function (a matrix with all the elements being 1).

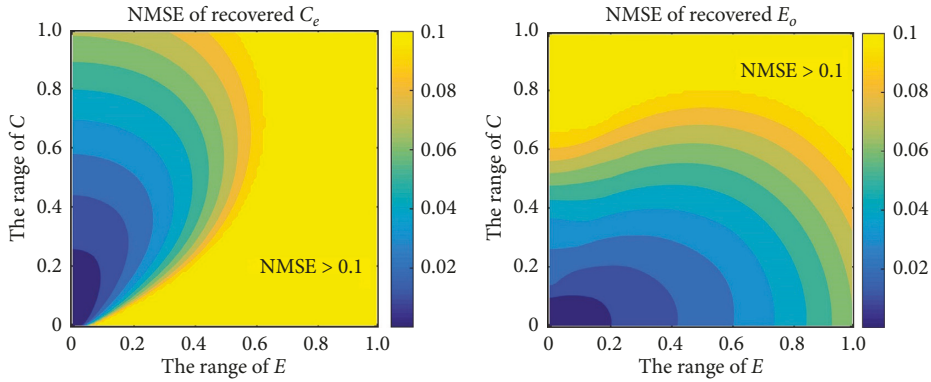


FIGURE 5: The recovery accuracy of C_e and E_o under different ranges of C and E . In the simulation, both C and E are set to be randomly smooth, and B is set to be a constant function (a matrix with all the elements being 1).

TABLE 3: Recovery accuracy of the method under different frequencies.

| f (GHz) | 0.3 | 0.4 | 0.5 | 0.6 | 0.7 | 0.8 |
|------------------------|-------|-------|-------|-------|-------|-------|
| NMSE of C_e (%) | 1.05 | 1.67 | 3.17 | 6.11 | 10.32 | 16.28 |
| RMS of δ_r (mm) | 0.136 | 0.169 | 0.236 | 0.330 | 0.429 | 0.540 |

Firstly, we discuss the practical challenge of bad feed positioning. The errors caused by bad feed positioning can have two conditions: location errors and pointing errors. Due to stable installation, it is believed the feed position and posture are both constant during the measurement process. Therefore, simulations are made by assuming position errors on X axis and Z axis for feed location errors and by introducing direction angle errors for feed pointing errors. According to simulation parameters shown in Table 2 and antenna deformation shown in Figure 5, the far-field intensity pattern is calculated in the PO method, after setting the feed position and direction. Then, reconstruct the given deformation through the proposed method and evaluate its accuracy performance by equation (17). The final results are listed in Tables 4–6.

From the above simulation results, it is seen the proposed method features a good tolerance to the feed position

TABLE 4: Accuracy performance under feed location errors on (X) axis.

| X-error (mm) | 0 | 0.5 | 1 | 1.5 | 2 |
|---------------------------|-------|-------|-------|-------|-------|
| RMS of δ_r (mm) | 0.130 | 0.168 | 0.257 | 0.360 | 0.470 |
| RMS of δ_{ro} (mm) | 0.054 | 0.117 | 0.222 | 0.333 | 0.443 |
| RMS of δ_{re} (mm) | 0.119 | 0.121 | 0.128 | 0.139 | 0.156 |

error: the accuracy decrease caused by X -axis location error happens mostly on reconstruction to the odd part of the deformation and Z -axis location error and pointing error decrease mostly the reconstruction accuracy of the even part of the deformation. Specifically, it is recommended the location error of antenna feed should be no more than 1 mm on X -axis and 5 mm on Z -axis, and the direction accuracy be better than 1.5° on feed pointing.

Secondly, we discuss the practical challenge of background data noise. In the evaluation to the performance of the method under background noise, it is considered the ideal intensity pattern is noiseless while the measured actual intensity pattern is with white Gaussian noise. Thus, in this numerical simulation, we add additive white Gaussian noise to the far-field amplitude pattern $|a|$ and then execute the developed algorithm to reconstruct the antenna surface deformation. For the added noise, signal-noise-ratio (SNR)

TABLE 5: Accuracy performance under feed location errors on (Z) axis.

| Z-error (mm) | -10 | -5 | 0 | 5 | 10 |
|---------------------------|-------|-------|-------|-------|-------|
| RMS of δ_r (mm) | 0.533 | 0.277 | 0.130 | 0.250 | 0.438 |
| RMS of δ_{ro} (mm) | 0.054 | 0.057 | 0.054 | 0.056 | 0.062 |
| RMS of δ_{re} (mm) | 0.530 | 0.271 | 0.119 | 0.254 | 0.434 |

TABLE 6: Accuracy performance under feed pointing angle errors.

| Angle-error ($^\circ$) | 0.5 | 1 | 1.5 | 2 | 2.5 |
|---------------------------|-------|-------|-------|-------|-------|
| RMS of δ_r (mm) | 0.129 | 0.147 | 0.205 | 0.305 | 0.438 |
| RMS of δ_{ro} (mm) | 0.052 | 0.058 | 0.069 | 0.082 | 0.097 |
| RMS of δ_{re} (mm) | 0.118 | 0.135 | 0.193 | 0.294 | 0.427 |

is introduced to describe the noise intensity. The following table (Table 7) demonstrates the accuracy performance of the technique under background noise with different SNR. From the simulation results, it is seen that the accuracy of the method is mostly dependent upon the reconstruction to the even part of the surface deformation, and an acceptable degree of the background noise should be $\text{SNR} > 50 \text{ dB}$.

5. Further Improvement

From the results listed in Table 3, it is seen that the performance of this method is highly dependent upon the test frequency. Allowable frequency should be less than 0.4 GHz. This dependence is caused by the much smaller ranges of C compared with E , which is essentially determined by the antenna geometric features. In practice, satellites are usually taken as the radio source, in which case the measurement frequency is supposed to be 1~12 GHz. Obviously, according to Table 3, an acceptable detection accuracy ($<0.2 \text{ mm}$) is unreachable because of high frequency when taking satellites as the source. Therefore, it is necessary to make further improvements to ensure the method applicable for high-frequency tests without too much degradation in the detection accuracy.

In relation with the preceding solution to C_e as shown in equation (11), the term $(\cos E_e \cos E_o)$ in equation (10) is approximated by 1 and thus ignored, compared with the original equation (7). However, by preserving the cosine, one may obtain a more accurate version of equation (10):

$$|a|_e \text{sign}(b) \approx F(A_{re}) \approx F(B(1 + C_e) \cos E_e \cos E_o). \quad (18)$$

From the above equation, we can solve a more accurate C_e , written as \bar{C}_e , to distinguish from the previously obtained one:

$$\begin{aligned} \bar{C}_e &\approx \frac{F^{-1}[|a|_e \text{sign}(b) - b]}{B \cos E_e \cos E_o} \approx \frac{C_e}{1 - ((E_e^2 + E_o^2)/2)} \\ &\approx C_e \left(1 + \frac{E_e^2 + E_o^2}{2}\right). \end{aligned} \quad (19)$$

Equation (19) implies that C_e solved from equation (11) is inaccurate, and the true value of C_e should be modified by multiplying a specific term that is also related with the aperture phase E . However, since we can only solve E_o , E_e

TABLE 7: Recovery accuracy of the method under background errors.

| SNR (dB) | 40 | 45 | 50 | 55 | 60 | Inf |
|---------------------------|-------|-------|-------|-------|-------|-------|
| RMS of δ_r (mm) | 0.281 | 0.200 | 0.153 | 0.139 | 0.132 | 0.127 |
| RMS of δ_{ro} (mm) | 0.135 | 0.072 | 0.050 | 0.038 | 0.035 | 0.034 |
| RMS of δ_{re} (mm) | 0.246 | 0.187 | 0.145 | 0.134 | 0.127 | 0.122 |

stays unknown and a more accurate C_e can never be obtained from equation (19). Comparing the accurate \bar{C}_e with the rough C_e , it also shows that the error on the right-hand side grows quadratically with E as frequency increases and consequently affects the accurate solution of C_e . This explains why the proposed method performs much worse in high-frequency measurement.

To make the method applicable for high test frequency, some means are desirable to eliminate the errors caused by E_e and E_o . Multifrequency scans may be a suitable solution. It is known that C_e does not vary with the frequency, while E_e and E_o do, in the same form. Therefore, one can finely eliminate the influence of E_e and E_o in the calculation of C_e by introducing more measurement frequencies. We have considered dual-frequency and tri-frequency scan in the simulation. It should be remarked that dual-frequency scan will not double the scanning time as the scanning of the two frequencies can be done at the same time. For the dual-frequency scan, assume for example that the two frequencies are f and $2f$ and denote the two solutions of C_e obtained from equation (11) by C_{e-f} , C_{e-2f} respectively. Based on the following relation obtained directly from equation (19),

$$C_e \approx \bar{C}_e \left(1 - \frac{E_e^2 + E_o^2}{2}\right). \quad (20)$$

An accurate C_e can be obtained as follows:

$$\begin{cases} \text{for frequency } f: C_{e-f} = \bar{C}_e \left(1 - \frac{E_e^2 + E_o^2}{2}\right), \\ \dots \\ \text{for frequency } 2f: C_{e-2f} = \bar{C}_e \left(1 - \frac{4E_e^2 + 4E_o^2}{2}\right), \end{cases} \quad (21)$$

$$\therefore \bar{C}_e = \frac{4C_{e-f} - C_{e-2f}}{3}.$$

Generally, introducing more frequency in the scan would contribute to more accurate solution of C_e . For instance, triple-frequency can finely eliminate the errors brought by both the square and quartic terms of E , and the corresponding accurate solution of C_e is

$$\bar{C}_e = \frac{32C_{e-f} - 14C_{e-2f} + 3C_{e-3f}}{21}. \quad (22)$$

Then, based on the simulation settings as described in Figure 4, we try to verify the improvement to the solution of C_e by using equations (21) and (22) in the case of dual- and triple-frequency scans. The corresponding simulation results are shown in Figure 6. By comparing the result of Figures 5 and 6, it can be seen that the proposed multifrequency scan is

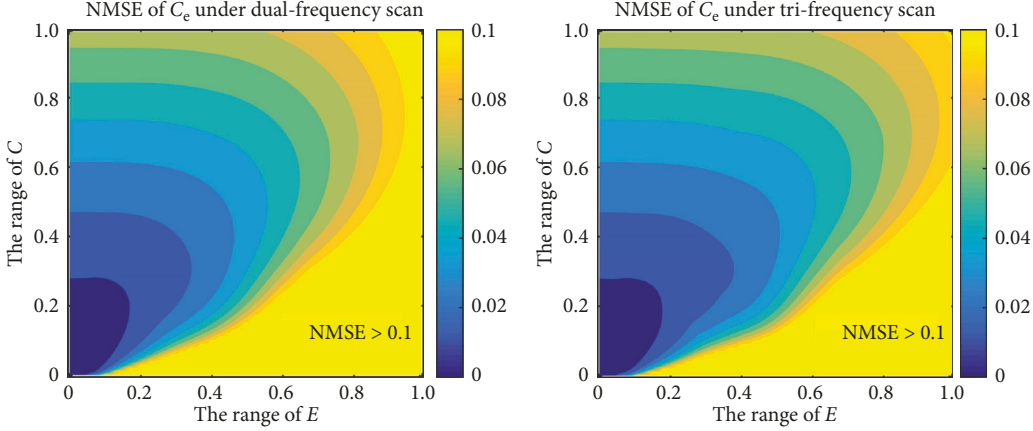
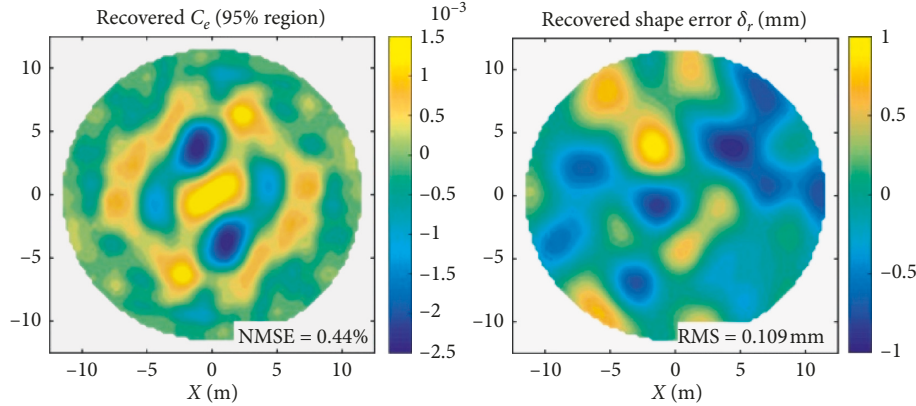
FIGURE 6: Improve the recovery accuracy to C_e by multifrequency scan.

FIGURE 7: Surface shape reconstruction accuracy improved by dual-frequency scan.

TABLE 8: Recovery accuracy of the method by dual-frequency scan.

| f (GHz) | 0.3 | 0.4 | 0.5 | 0.6 | 0.7 | 0.8 |
|------------------------|-------|-------|-------|-------|-------|-------|
| NMSE of C_e (%) | 0.44 | 0.46 | 0.46 | 0.50 | 0.56 | 0.70 |
| RMS of δ_r (mm) | 0.110 | 0.111 | 0.111 | 0.113 | 0.117 | 0.125 |

effective to improve the recovery of C_e . Figure 6 also shows that dual-frequency scan (left) is already a fairly good scheme, but triple-frequency scan (right) makes little more help over the former.

To show further the effect of the proposed dual-frequency scan to reconstruct the surface shape error of a large reflector antenna, we have also made some numerical simulations based on the PO method to generate the needed far-field intensity patterns under two different frequencies. We first apply equation (11) to obtain two inaccurate C_e , then apply equation (21) to achieve an improved result of C_e , and finally solve the antenna surface shape based on equation (12). As shown in Figure 7, compared with the results by the single-frequency scheme, the NMSE values of C_e drops from 1.05% to 0.44%, and the final RMS of δ_r drops from 0.136 mm to 0.109 mm.

Moreover, the dual-frequency scheme exhibits a good tolerance to the measurement frequency. As shown in

Table 8, both the NMSE and RMS values no longer increase rapidly, but very slightly with the measurement frequency.

6. Conclusion

An effective method for measuring the surface shape of reflector antennas by single focused far-field intensity has been proposed. Based on the fact that the deformed surface shape causes change not only in the phase but also in the amplitude, it has been proved that a complete shape recovery is possible from single focused far-field intensity. Unlike traditional phase based surface shape detection scheme, amplitude retrieval and phase retrieval are combined in the process. The “odd-phase” and the “even-amplitude” are solved directly so that the “odd-shape” and the “even-shape” are recovered simultaneously, and at last complete surface shape detection is achieved from single focused far-field intensity.

Numerical simulations based on a 25 m radio telescope showed the effectiveness of the algorithm at low frequencies; also, a good tolerance of the proposed technique to feed location/pointing errors and background data noise has been verified through numerical simulations. Further improvement is also studied so that the method can be applicable to higher frequency measurements. It is shown that

dual-frequency scheme can greatly improve the recovery accuracy to C_e , as well as to the surface shape δ_r . In short, our work is promising for detecting surface shape of large reflector antennas with single in-focus far-field intensity.

Data Availability

The generated data of the designed surface shape error and the corresponding far-field intensities used in the simulations of this study are available from the corresponding author upon request.

Conflicts of Interest

The authors declare that there are no conflicts of interest regarding the publication of this paper.

Acknowledgments

The authors thank the financial support from National Basic Research Program of China (973 Program) (2015CB857100) by the Ministry of Science and Technology of the People's Republic of China (501100002855).

References

- [1] J. Ruze, "Antenna tolerance theory—a review," *Proceedings of the IEEE*, vol. 54, no. 4, pp. 633–640, 1966.
- [2] Y. Rahmat-Samii, "Microwave holography of large reflector antennas—simulation algorithms," *IEEE Transactions on Antennas and Propagation*, vol. 33, no. 11, pp. 1194–1203, 1985.
- [3] J. R. Fienup, "Phase retrieval algorithms: a personal tour [invited]," *Applied Optics*, vol. 52, no. 1, pp. 45–56, 2013.
- [4] D. Morris, "Simulated annealing applied to the Misell algorithm for phase retrieval," *IEE Proceedings on Microwaves, Antennas and Propagation*, vol. 143, no. 4, p. 288, 1996.
- [5] P. Netrapalli, P. Jain, and S. Sanghavi, "Phase retrieval using alternating minimization," *IEEE Transactions on Signal Processing*, vol. 63, no. 18, pp. 4814–4826, 2015.
- [6] B. Nikolic, R. M. Prestage, D. S. Balser, C. J. Chandler, and R. E. Hills, "Out-of-focus holography at the green bank telescope," *Astronomy & Astrophysics*, vol. 465, no. 2, pp. 685–693, 2007.
- [7] D. Morris, M. Bremer, G. Butin et al., "Surface adjustment of the IRAM 30 m radio telescope," *IET Microwaves, Antennas & Propagation*, vol. 3, no. 1, pp. 99–108, 2009.
- [8] R. A. Gonsalves, "Small-phase solution to the phase-retrieval problem," *Optics Letters*, vol. 26, no. 10, pp. 684–685, 2001.
- [9] M. Li, X.-Y. Li, and W.-H. Jiang, "Small-phase retrieval with a single far-field image," *Optics Express*, vol. 16, no. 11, pp. 8190–8197, 2008.
- [10] B. Dong, G. Jia, and R. Wang, "Hybrid phase retrieval from a single defocused image," in *Proceedings of the 2015 International Conference on Optical Instruments and Technology: Optoelectronic Imaging and Processing Technology*, vol. 9622, SPIE, Beijing, China, August 2015.
- [11] A. Polo, S. F. Pereira, and P. H. Urbach, "Experimental demonstration of phase retrieval from a single defocused intensity measurement in the approximation of small aberrations," in *Imaging and Applied Optics*, OSA Technical Digest (Online), AW1B, Washington, DC, USA, 2013.
- [12] J. Huang, H. Jin, Q. Ye, and G. Meng, "Surface deformation recovery algorithm for reflector antennas based on geometric optics," *Optics Express*, vol. 25, no. 20, pp. 24346–24361, 2017.
- [13] Y. Liu, F. Huang, Q. Zhang, J. Yuan, and T. Dong, "Calculations of radiation characteristics of reflector antennas with surface deformation and perforation," *Computers & Mathematics with Applications*, vol. 61, no. 8, pp. 2349–2352, 2011.

